ADVANCED MATERIALS
www.advmat.de

Artificial Synapses Emulated by an Electrolyte-Gated Tungsten-Oxide Transistor

Jing-Ting Yang, Chen Ge, Jian-Yu Du, He-Yi Huang, Meng He, Can Wang, Hui-Bin Lu, Guo-Zhen Yang, and Kui-Juan Jin**

Considering that the human brain uses ≈10^{15} synapses to operate, the development of effective artificial synapses is essential to build brain-inspired computing systems. In biological synapses, the voltage-gated ion channels are very important for regulating the action-potential firing. Here, an electrolyte-gated transistor using WO_3 with a unique tunnel structure, which can emulate the ionic modulation process of biological synapses, is proposed. The transistor successfully realizes synaptic functions of both short-term and long-term plasticity. Short-term plasticity is mimicked with the help of electrolyte ion dynamics under low electrical bias, whereas the long-term plasticity is realized using proton insertion in WO_3 under high electrical bias. This is a new working approach to control the transition from short-term memory to long-term memory using different gate voltage amplitude for artificial synapses. Other essential synaptic behaviors, such as paired pulse facilitation, the depression and potentiation of synaptic weight, as well as spike-timing-dependent plasticity are also implemented in this artificial synapse. These results provide a new recipe for designing synaptic electrolyte-gated transistors through the electrostatic and electrochemical effects.

With the rapid development of artificial intelligence, the need for a variety of intelligent tasks, ranging from real-time big data analytics, motor control, to visual and auditory recognition, has exploded in the whole world.[1] Although von Neumann-based digital-logic computers excel in performing numerical calculation, they often require complex algorithms and consume significant power for executing these intelligent tasks.[2–4] For example, the IBMs supercomputer (Blue Gene/P) consumes ≈2.9 MW of power to emulate 4.5% of human brain by software simulations, while human brain consumes only ≈20 W of power to do the same tasks.[4,5] Human brain, consisting of ≈10^{11} neurons with ≈10^{15} synapses interconnecting with each other, is particularly efficient at solving complex and unstructured problems.[6–8] The high efficiency of human brain is due to the synaptic-activity-dominated operation of the neural network, through which information processing and storage can occur simultaneously. Therefore, the emulation of synapses is important to realize efficient artificial-neuromorphic computers.

The voltage-gated ion migration plays a key role in the signal transmission of synapses by controlling the release of neurotransmitters in a presynaptic neuron and the formation of current to alter the conductance of a postsynaptic neuron (**Figure 1**a). When a positive electrical signal arrives in a presynaptic neuron, it will open the voltage-gated calcium channels and generate a Ca^{2+} flow into the neuron. A rapidly increasing concentration of Ca^{2+} triggers the release of neurotransmitters, which will dock with receptors onto the postsynaptic neuron. If enough neurotransmitters dock with receptors, an electric stimulus will respond in postsynaptic neuron. In this way, information is transmitted from a presynaptic neuron to a postsynaptic neuron.[9] The strength of the connection between neurons is defined as synaptic weight. The change of synaptic weight is known as "synaptic plasticity" and represents the foundation of learning and memory in neuronal systems. Among many synaptic properties, short-time plasticity (STP) and long-term plasticity (LTP) are the most prominent forms of plasticity observed in mammalian brains. STP is a temporal enhancement of synaptic weight, which quickly decays to its initial state. LTP, on the other hand, is considered as a persistent modification of synaptic weight that lasts from minutes to several weeks.[6,10]

Artificial synaptic functions can be mimicked in nonvolatile memory devices, where resistance switching related with an ionic migration process emulates synaptic weight. Two-terminal memristors such as resistive random access memory,[11,12] ferroelectric random access memory,[13] and phase change random access memory[14] have been extensively investigated as artificial synaptic devices. These devices enabled several important advances for image recognition and data classification.[15,16] In addition to the most studied two-terminal devices,

Dr. J.-T. Yang, Prof. C. Ge, J.-Y. Du, H.-Y. Huang, M. He, Prof. C. Wang, Prof. H.-B. Lu, Prof. G.-Z. Yang, Prof. K.-J. Jin
Beijing National Laboratory for Condensed Matter Physics
Institute of Physics
Chinese Academy of Sciences
Beijing 100190, China
E-mail: gechen@iphy.ac.cn; kjjin@iphy.ac.cn
Dr. J.-T. Yang, H.-Y. Huang, Prof. G.-Z. Yang, Prof. K.-J. Jin
School of Physical Sciences
University of Chinese Academy of Science
Beijing 100049, China
Prof. G.-Z. Yang, Prof. K.-J. Jin
Collaborative Innovation Center of Quantum Matter
Beijing 100190, China
The ORCID identification number(s) for the author(s) of this article can be found under https://doi.org/10.1002/adma.201801548.

DOI: 10.1002/adma.201801548

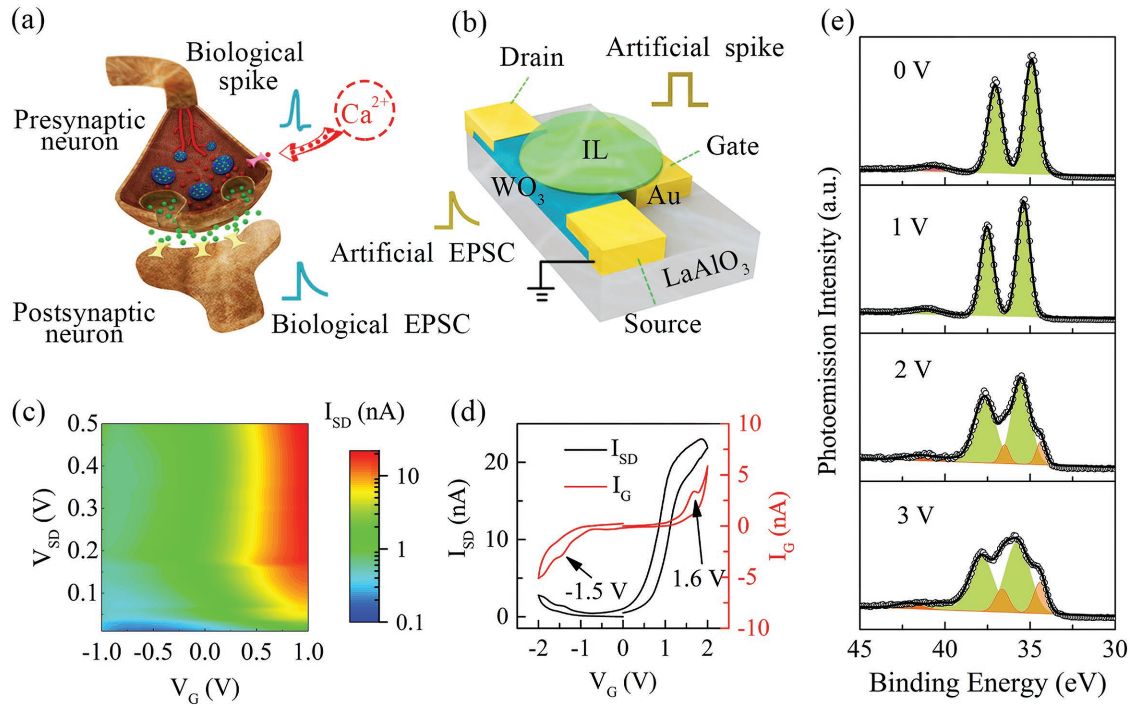

Figure 1. Device architecture and electronic properties of the WO_3-based transistor. a) Schematic illustration of a neural synapse. b) Schematic diagram of three-terminal synaptic transistor, in which the gate electrode emulates the presynaptic input terminal, with source and drain electrodes mimicking the postsynaptic output terminal. c) Source–drain current on the upper part of hysteresis curves (Figure S3a, Supporting Information) as a function of both V_G and V_{SD}. The current is plotted as a color map with a logarithmic scale. d) Transfer curves of the WO_3 transistor measured with V_{SD} = 50 mV. Two small peaks observed in I_G–V_G curve indicate a hydrolysis reaction occurring in ionic liquid. e) W 4f core-level XPS of the pristine sample ("0 V") and samples with different gate voltages. "1 V," "2 V," and "3 V" samples are gated with 1 V 20 h, 2 V 20 h, and 3 V 4 h, respectively. The experimental data are shown as open circles and fitted with solid lines. The fitted components W_a (green) and W_b (orange) are displayed in different colors.

electrolyte-gated three terminal devices have been proposed for synaptic emulation recently.[17–22] In these devices, the conductivity of the channel between source and drain electrodes is regarded as synaptic weight. The voltage pulses applied to the gate electrode are usually regarded as presynaptic spikes, which can affect the channel conductivity and mimic synaptic plasticity. Moreover, electrolyte gating can harness the huge electric double layer (EDL) capacitance and possible electrochemical reaction, which has the potential to decrease the gating voltage, and then reduce the power consumption.[23] In other words, electrolyte-gated transistors offer an alternative approach for efficient artificial synapse.

Tungsten oxide (WO_3), which consists of corner-sharing $[WO_6]$-octahedral structures, can be regarded as a pseudo-perovskite oxide with absent A-site cations.[24] This absence of A-site cations provides sufficient interstitial space for ion intercalation and extraction, which makes tungsten oxide an excellent model material for artificial synaptic devices. Consequently, it can contribute to understand the underlying mechanism of any electrolyte-gating-induced phenomena. Moreover, WO_3 is an insulator with an unoccupied 5d conduction band, and it can become metallic via ion intercalation. Utilizing this feature, several research groups reported that electrolyte gating can modify the transport properties of WO_3.[25–27] This characteristic of WO_3 provides an opportunity to emulate the biological Ca^{2+} dynamics[28] and thus pave the way to robust artificial synaptic transistors.

In this paper, we describe a synaptic transistor with an electrolyte-gated WO_3 film. It is the first example for harnessing WO_3 epitaxial films in artificial synaptic transistors. We investigate the working principle of the electrolyte-gated WO_3 transistor, combining electrical transport measurements, X-ray photoelectron spectroscopy (XPS), Raman spectroscopy, transmission spectroscopy, and secondary ion mass spectrometry (SIMS). Then we implement the synaptic functions STP, LTP, paired-pulse facilitation (PPF), and spike-timing-dependent plasticity (STDP) in the synaptic transistor based on the proposed mechanism. These results provide a deep insight into the emulation of artificial synapses and enable a new approach to mimic synaptic functions.

We designed an electrolyte-gated transistor architecture to emulate the functions of a biological synapse (Figure 1b). Epitaxial films of high-quality WO_3 were prepared on a $LaAlO_3$ (LAO) substrate using pulse laser deposition (PLD). We carried out X-ray diffraction (XRD), reciprocal space mapping (RSM), and atomic force microscopy (AFM) experiments. All measurements indicate a good crystalline quality of WO_3 epitaxial thin films (Figures S1 and S2, and Note S1, Supporting Information). More details about the film growth procedure can be found elsewhere.[24] The WO_3 thin films were patterned in a micrometer-scale channel with a coplanar gate electrode (see the Experimental Section for details). Subsequently, as-received ionic liquid (IL) N,N-diethyl-N-(2-methoxyethyl)-N-methylammonium bis-(trifluoromethylsulphonyl)-imide (DEME-TFSI) was dropped on the channel and coplanar electrodes to serve as the electrolyte-gating medium. We used this IL due to its powerful regulation ability.[29] The transfer curve was measured by sweeping gate voltage (V_G) from 0 to 1.0 V, 1.0 to −1.0 V, and then back to 0 V (Figure S3a, Supporting Information). During the sweep, the source terminal was always grounded. The electrolyte-gated WO_3 structure exhibits a typical transistor behavior (Figure 1c). The channel conduction opens under a positive gate bias, while the channel conduction closes for a negative gate bias. The drain current increases linearly with drain voltage (V_{SD}) at first before it gradually approaches a saturated value, similar to a typical output curve of a transistor (Figure S3b, Supporting Information). The source–drain current (I_{SD}) is at least 20 times larger than the gate current (I_G) when V_G is higher than 0.15 V (Figure S3c, Supporting Information). In other words, there is a negligible effect of I_G on the device performance. The threshold voltage value of the electrolyte-gated WO_3 transistor is 0.52 V (Figure S4, Supporting Information). The volatile channel resistance state can be immediately reverted to the pristine state after removing the gate bias, which suggests a pure electrostatic effect from EDL. If we increase the V_G to 2 V, the positive gating modulation of the channel resistance becomes more pronounced. Interestingly, small peaks near 1.6 V appear in I_G curves (Figure 1d). These peaks can be associated with the hydrolysis reaction of the trace water contaminated in ILs according to several recent studies.[30,31] In such cases, water molecules could dissociate into small protons and hydroxy groups, which can readily penetrate into the interstitial positions of oxide lattices. The change of the channel resistance during high positive gating can last for at least several hours even after IL was washed off, which indicates nonvolatile behavior (Figure S5, Supporting Information).

To explore the underlying mechanism of this gating-induced phenomenon, we probed the valence state of both the W ion and valence-band spectrum for various positive gate voltages using XPS measurements. Four samples labeled “0 V,” “1 V,” “2 V,” and “3 V” denote the pristine, +1 V gated, +2 V gated, and +3 V gated WO_3 films, respectively. Pt wire was pasted on the WO_3 thin films to serve as one electrode, and a screwed Au wire was used as the other electrode. The samples were entirely covered with IL. ILs were washed off with isopropanol after gating. Figure 1e shows the W 4f core-level XPS for four samples. The W 4f spectra are fitted using two components W_a (marked in green) and W_b (marked in orange), where W_a represents W^{6+}, and W_b denotes a lower valence of the W ions. Clearly, the W 4f spectra for the “0 V” and “1 V” samples contain only W_a, which corresponds to W^{6+} atoms in the $[WO_6]$-octahedral coordination.[32] The W 4f spectra of the “2 V” and “3 V” samples consist of W_a and W_b, and both components split into a $4f_{5/2}$ and $4f_{7/2}$ spin–orbit doublet. Component W_b, with a lower binding energy originates from the defective $[WO_6]$-octahedra possibly induced by ion intercalation. The ratio of component W_b to component W_a in the “3 V” sample is much larger than that in the “2 V” sample, indicating that more tungsten ions change from W^{6+} into W^{5+} or even W^{4+}. The valence band consists of a hybridized orbital between the O 2p and W 5d states (Figure S6, Supporting Information). The valence band state of the W ions hardly changes, even after 20 h with 1 V gate bias. For the “2 V” and “3 V” samples, the valence band broadens, and a peak near the Fermi level can be observed. This suggests an insulator to metal transition via IL gating. Insulator to metal transition was further confirmed by transport measurement (Figure S5, Supporting Information). The electron doping density obtained via Hall measurements can reach about 10^{16} cm^{-2} for the metallic “3 V” sample. Both the W 4f core level and the valence band photoemission spectra of the “2 V” and “3 V” samples are consistent with what were observed in hydrogen tungsten bronze H_xWO_3.[33,34] XPS results show that the nonvolatile resistance change is closely related to the valence-state change of the W ions, probably due to ion intercalation.

Raman spectra reveal a structural transformation during valence changes (Figure S7, Supporting Information). In the “0 V” sample, the three main vibrational modes of WO_3 (at ≈274, ≈718, and 804 cm^{-1}) are consistent with a monoclinic WO_3 structure.[35] The Raman spectra of the “1 V” sample are almost identical with the “0 V” sample, showing no change for 1 V. For the “2 V” sample, the peak at 804 cm^{-1} decreases slightly. Clearly, the peaks at 274 and 718 cm^{-1} are strongly suppressed, and the peak intensity at ≈804 cm^{-1} decreases with shifting to a higher frequency for the “3 V” sample. These changes indicate that a structural transformation toward a higher symmetric phase occurs in the “3 V” sample, which is consistent with known H-doping-induced structural transitions.[36] In addition, we observed an electrochromic effect for the “2 V” and “3 V” samples. The optical transmission spectrum shows that the samples “0 V” and “1 V” are transparent, while the “2 V” sample increases its absorptivity in the visible light region (Figure S8, Supporting Information). For sample “3 V,” the absorptivity was significantly enhanced for both the visible and infrared spectrum. In addition, the color changes from transparent to deep blue, which is consistent with the electrochromic process to form H_xWO_3.[37] The optical absorption in the colored films is caused by transitions between the W^{6+} and W^{5+} states.[38] The above measurements show that the nonvolatile modulation of physical properties only occurs in the “2 V” and “3 V” samples. In these samples, V_G should be higher than the threshold voltage for a hydrolysis reaction. The formed phase is very similar to H_xWO_3. Therefore, we speculate that the changes of valence state and conductivity in WO_3 films are associated with proton intercalation from water contaminated in the IL.

In order to shed more light on the role of the proton in the gating process, we performed time-of-flight secondary ion mass spectrometry (TOF-SIMS) on this series of samples to identify the depth profiles of the protons (Figure S9, Supporting Information). The signal for H^+ is normalized through dividing by the intensity of W ion. The normalized H^+ signal shows a higher hydrogen content when the positive V_G increases. There are almost no protons in the “0 V” and “1 V” samples. However, there are many protons in the “3 V” sample. This leads to a very high electron density, which was revealed in the measured transport data. Thus, we can conclude that the nonvolatile modulation is caused by the proton evolution during the positive gating process.

The volatile and nonvolatile resistance changes in the IL-gated WO_3 transistor can be explained as follows. For a positive V_G that is lower than the threshold value of the hydrolysis reaction (V_T), DEME+ (TFSI–) ions in ILs accumulate at the IL/channel (IL/gate) interfaces to form EDLs (**Figure 2**a). The introduction of electrons through EDL can effectively decrease channel resistance. Once V_G is removed, cations and anions in ILs will relax and mix together in seconds (Figure 2b). Correspondingly, the volatile channel resistance will revert to the pristine value accompanied by the ion relaxation. If a positive V_G higher than V_T is applied, the water molecules contaminated in ILs can dissociate into protons and hydroxyls (Figure 2c). In addition to the EDL effect, the protons can be inserted into the absent A-site of WO_3 via the strong electric field of EDL (Figure 2c). The proton intercalation causes a valence change from W^{6+} to W^{5+}, and the formation of a stable H_xWO_3 phase. Even with the voltage removed, the nonvolatile resistance state from the H_xWO_3 phase is maintained (Figure 2d). The ionic modulation of the channel resistance resembles the transmission process in biological synapses. In other words, the synaptic behavior can be naturally emulated through the volatile and nonvolatile process in an IL-gated WO_3 transistor. The volatile channel modulation for a low V_G is analogous to the concept of a short-term memory (STM), while the nonvolatile channel modulation for a high V_G can be utilized to mimic long-term memory (LTM).

For the above reasons, we used gate pulse voltages (presynaptic spikes) of 0.6 V to emulate STM. A presynaptic spike applied to the gate electrode triggers an excitatory postsynaptic current (EPSC) in the WO_3 channel. **Figure 3**a shows a typical EPSC response of this synaptic transistor triggered by a presynaptic spike (0.6 V, 70 ms). The current responses are monitored with a small V_{SD} of 0.3 V. The EPSC shows a fast increase after applying the presynaptic pulse, and it reaches a peak value of ≈1.73 nA. Then, it decays gradually to reach a resting current of ≈1.33 nA in ≈750 ms. Such behavior is quite similar to the EPSC process of STM in a biological excitatory synapse. The energy consumption calculated with $I_{peak} \times t_d \times V_{SD}$ is about 36 pJ, where I_{peak}, t_d, and V_{SD} represent the peak value of the EPSC, the duration time of the pulse voltage, and the source–drain voltage, respectively.[39] The energy consumption is much lower than that of an artificial synapse based on conventional CMOS circuits (≈900 pJ per stimulation), and comparable to that of three-terminal electrolyte-gated synaptic devices.[19,40,41] It is reasonable to estimate that we can reduce the energy consumption to sub-pJ level if the spike duration can be reduced to sub-microsecond level.

Figure 3b shows EPSC induced by presynaptic pulses with different durations (V_G = 0.6 V, V_{SD} = 0.3 V). The amplitudes of EPSC increase for longer presynaptic pulses. All EPSCs gradually decay and approach the resting current, suggesting a short-term property. Such ion-migration-induced EPSC decay is similar to the memory retention (forgetting curve) in human brain.[42] The memory retention of the WO_3-based synapses is in agreement with the commonly used forgetting curve $y = b \times t^{-m}$, where y, t, b, and m represent memory retention, time, the fitting constant for scaling, and the power function rate, respectively (Figure S10 and Table S1, Supporting Information).[10] Here, the power function rate m is a value that is relative to the retention time, in which a smaller decay rate represents a larger retention time. The retention time increases with increasing the duration time of the spike. STP can also be modulated using different frequencies for spike stimulations. Figure S11 (Supporting Information) shows the EPSCs recorded in response to the stimulus train for different frequencies. The stimulus train at each frequency consists of 10 pulses with a voltage of 0.6 V and a duration time of 70 ms. To clearly exhibit the current change recorded for each frequency, we plotted the EPSCs as a function of the stimulation number (Figure 3c). The relative change of currents versus stimulation number is shown in Figure 3d. The EPSC peak value increases with increasing frequency of the stimulus train. This implies a synaptic plasticity in our WO_3-based transistor. Paired-pulse facilitation (PPF) and post-tetanic potentiation (PTP) are two important forms of STP.[9,19] They play important roles in decoding temporal information in auditory or visual signals.[22,43] PPF and PTP depict a phenomenon, where EPSCs are evoked by the second and the tenth pulse, respectively. They are both larger than the first pulse if the time interval between two pulses is small. Our synaptic transistor can emulate PPF and PTP as the following equations[43]

$$\mathrm{PPF} = (I_2 - I_1)/I_1 \times 100\% \tag{1}$$

$$\mathrm{PTP} = (I_{10} - I_1)/I_1 \times 100\% \tag{2}$$

where I_1, I_2, and I_{10} are the currents recorded immediately after the first, the second, and the tenth voltage stimulus, respectively. The maximum PPF and PTP values are ≈6.8 and 18.2%, respectively (Figure 3e). A typical exponential dependence of the synaptic plasticity was found on both PPF and PTP (Figure 3e). We fitted the curves with a double-exponential function $1 + C_1 \exp\left(\frac{-t}{\tau_1}\right) + C_2 \exp\left(\frac{-t}{\tau_2}\right)$, where t is the pulse interval time, C_1 and C_2 are the initial facilitation magnitudes, and τ_1 and τ_2 are the characteristic relaxation times.[22] For fitting PPF, we used C_1 = 8.1%, C_2 = 4.2%, τ_1 = 57 ms, τ_2 = 537 ms. For fitting PTP, we used C_1 = 16.1%, C_2 = 13.1%, τ_1 = 64 ms, τ_2 = 759 ms. These relaxation time constants are consistent with those in a biological synapse.[22] PPF and PTP behaviors in the WO_3-based synaptic transistor can be explained as follows. When the pulse interval is shorter than the relaxation time, the accumulated cations at the interface by the first pulse cannot be fully recovered. The accumulated cations become more with the application of the second pulse, and thus the channel conduction induced by EDL is enhanced. Then, we can achieve a gradual increase of the channel conduction with increasing pulse numbers.

LTP was realized by applying a spike pulse larger than the threshold voltage of the hydrolysis reaction. **Figure 4**a shows EPSC obtained by applying a gate pulse with an amplitude of 1.8 V and a duration time of 210 ms. The source–drain currents are monitored with a small voltage of 0.3 V (V_{SD} = 0.3 V). The current reaches a peak voltage of ≈3.83 nA and cannot decay to its pristine value after 40 s, suggesting a long-term memory effect. The retention and peak currents triggered by the gate pulse increase with increasing the pulse width (Figure 4b). The long-term memory can also be described using different frequencies for the spike stimulation (Figure S12, Supporting Information). By changing the frequency from 0.05 to 2.4 Hz,

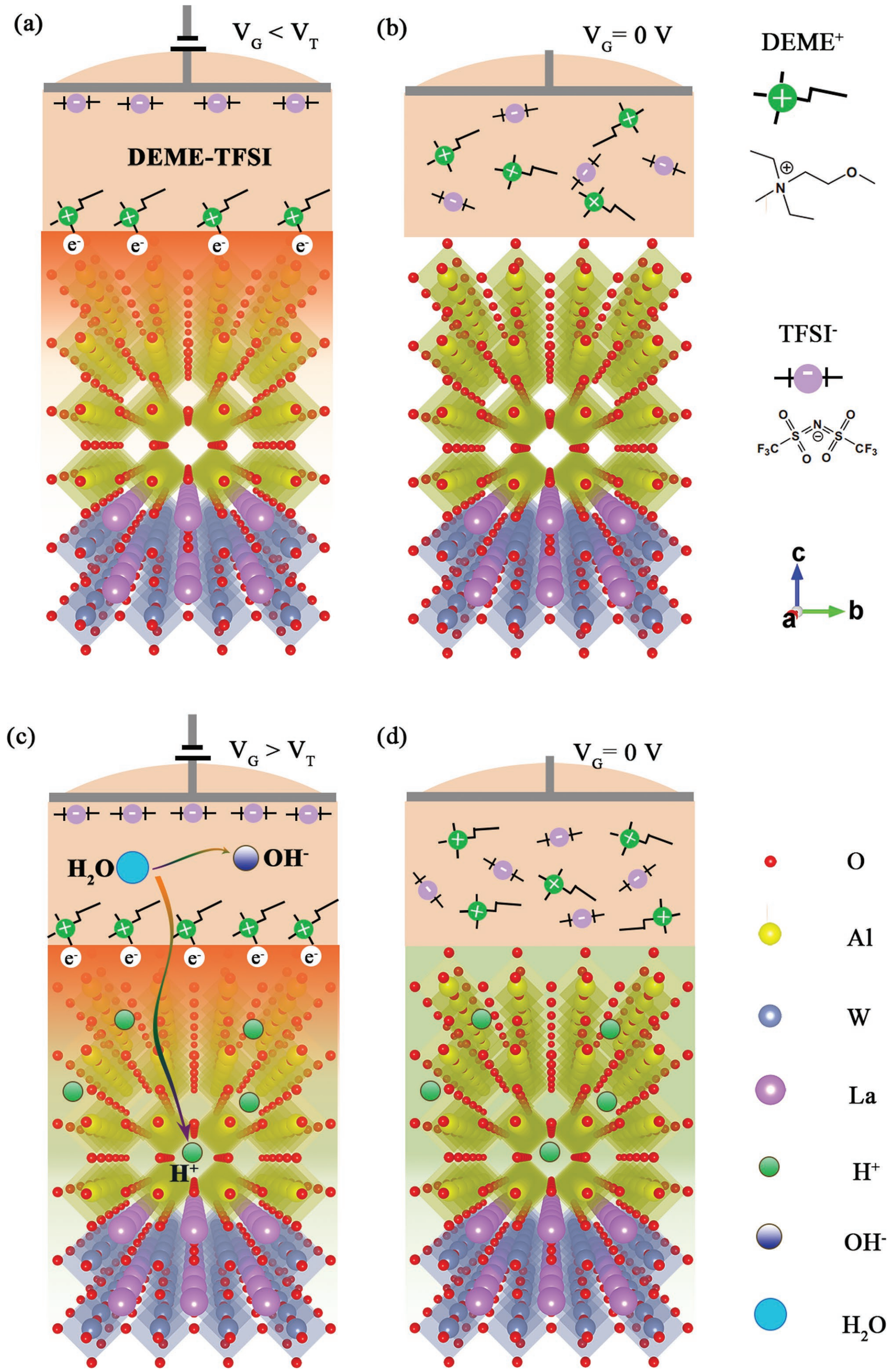

Figure 2. Schematic of a,c) ion migration and b,d) relaxation for the gating dynamics. a) By applying a positive V_G lower than the threshold value of the hydrolysis reaction (V_T), an electric double layer (EDL) is formed at the IL/channel interface. b) After removing V_G, the accumulated cation $DEME^+$ is mixed together with the anion $TFSI^-$, and the electrons induced by EDL decay simultaneously. c) By applying a positive V_G larger than V_T, the contaminated water in IL could dissociate into H^+ and OH^- besides the formation of EDL. The small protons can intercalate into WO_3 film to form a H_xWO_3 phase. d) After removing V_G, the accumulated cation $DEME^+$ was mixed together with the anion $TFSI^-$, while the H_xWO_3 phase can maintain.

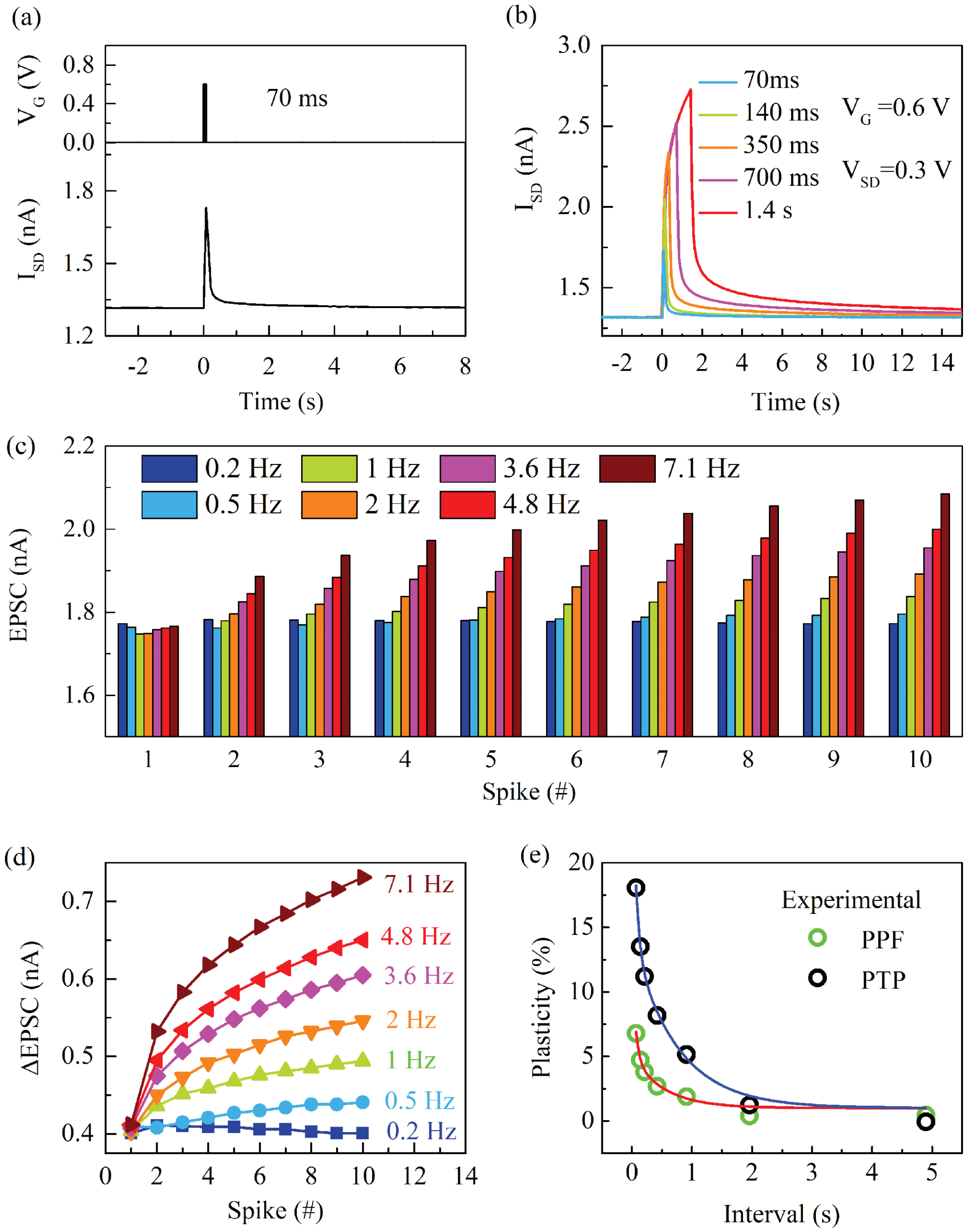

Figure 3. Short-term plasticity of the WO_3 artificial synapses. a) Excitatory postsynaptic current triggered by a presynaptic spike ($V_G = 0.6$ V, $t_d = 70$ ms, $V_{SD} = 0.3$ V). b) EPSCs triggered by gate pulses ($V_G = 0.6$ V) with different duration times. c) Current and d) current change with 10 pulse stimulations ($V_G = 0.6$ V, $t_d = 70$ ms) at different frequencies. The selected frequencies are the reciprocal of the multiples of t_d. The current responses are monitored with a small voltage of 0.3 V. e) PPF and PTP curves fitted with an exponential function.

EPCSs increase with increasing frequency (Figure 4c). The relative residual EPSCs after 60 s increase for higher frequencies (Figure S13, Supporting Information), which indicates that an LTP occurs in our artificial synapse.

LTP usually includes long-term potentiation and long-term depression. Long-term potentiation is widely considered the mechanism that underlies learning and memory in biological systems.[20] Long-term potentiation tends to enhance the electrical response of neurons. To demonstrate long-term potentiation, we applied ten consecutive gate spikes in the synaptic transistor, with an amplitude of 1.8 V, a pulse width of 210 ms, and an interval of 210 ms (Figure 4d). After the triggered spikes, the maximus EPSC increases by ≈4.2 times compared with resting current, and the retention current after 100 s was ≈1.7 times the resting current (Figure 4d). In contrast, long-term depression is used to selectively weaken specific synapses and prevent encoding new information.[20] It tends to decrease the electrical response which can be realized by applying negative gate spikes (Figure S14, Supporting Information). The synaptic potentiation and depression are mimicked by consecutive positive (1.8 V, 210 ms) and negative spikes (–1 V, 210 ms), respectively (Figure 4e). The EPSC amplitude gradually increases with the positive gate spike (potentiation), while the EPSC amplitude decreases to the initial value with the negative

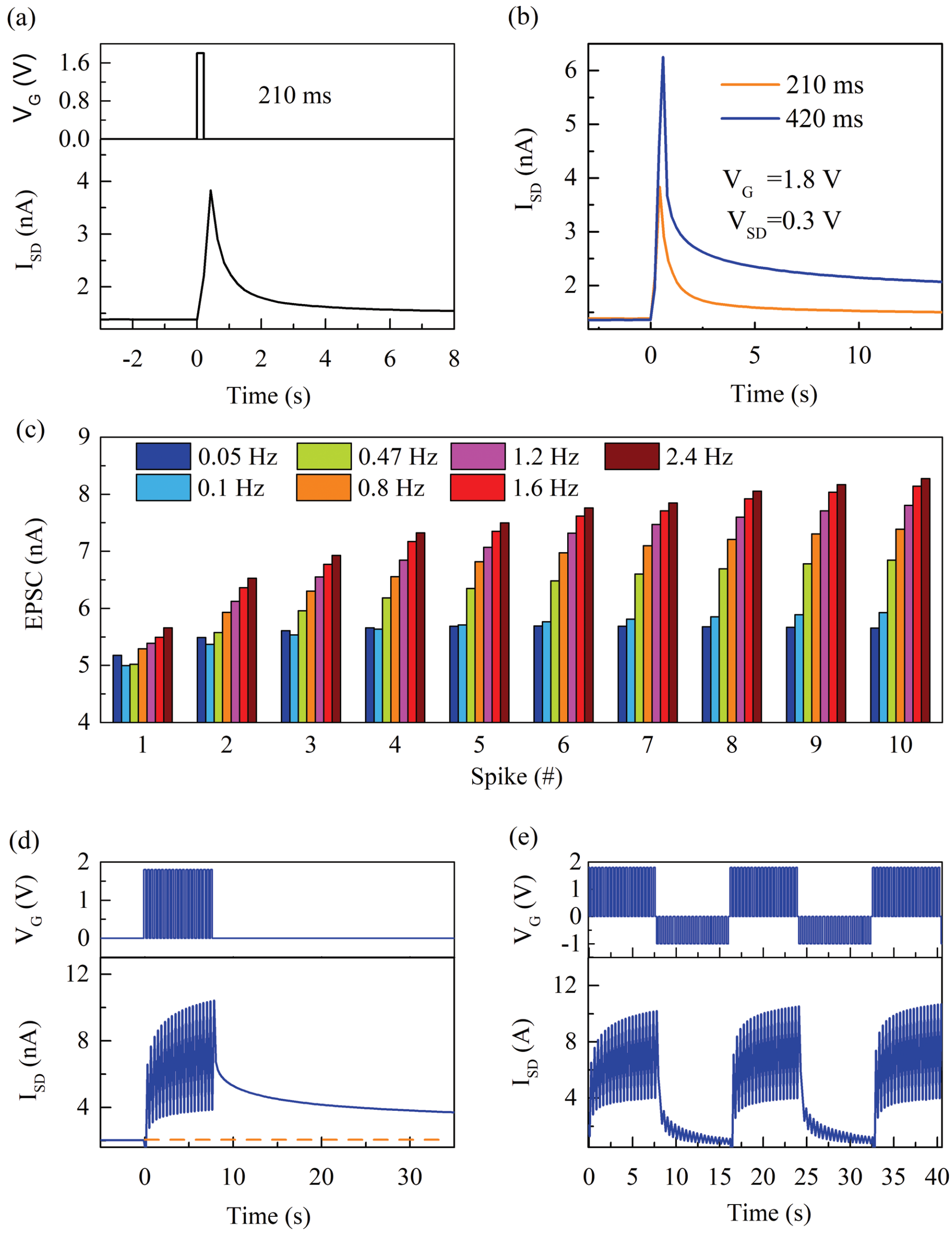

Figure 4. Long-term plasticity of WO_3 artificial synapses. a) Excitatory postsynaptic current triggered by a presynaptic spike (V_G = 1.8 V, t_d = 210 ms, V_{SD} = 0.3 V). b) EPSCs triggered by a presynaptic spike (V_G = 1.8 V) with different duration times. c) EPSCs as a function of stimulation number and frequencies (V_G = 1.8 V, t_d = 210 ms). The selected frequencies are the reciprocal of the multiples of t_d. The current responses are monitored with a small voltage of 0.3 V. d) Long-term potentiation mimicked by a stimulus train with 10 pulses (V_G = 1.8 V, t_d = 210 ms). e) Synaptic potentiation and depression.

gate spike (depression). The results imply that the present device can simulate LTP behavior of synapses.

In order to demonstrate how short-term and long-term memory alternately affect the concrete psychological behavior,[10] the memorization of three images in a 5 × 7 synapse array was initiated (**Figure 5**a). The images of letters "C," "A," and "S" were successively inputted into the synapse array using 30 pulses for each, with an amplitude of 0.6, 1.8, and 0.6 V. Both duration and interval time of the pulse were 210 ms, while the interval time for each stimulus train was 10 s. The letters "C" and "S" were memorized in STM mode, and the letter "A" was memorized in LTM mode. The positions of the green and red lines represent the events of the last pulse and 5 s after the last pulse, respectively. To clearly display the response, a typical electrical training curve, which corresponds to the pixel in the first row and the second column of the synapse array, is shown in Figure 5b. This pixel undergoes all three stimulus trains. After training with the letter "C," the temporary current enhancement in the channel immediately decays to reach the initial state. After training with the letter "A," a

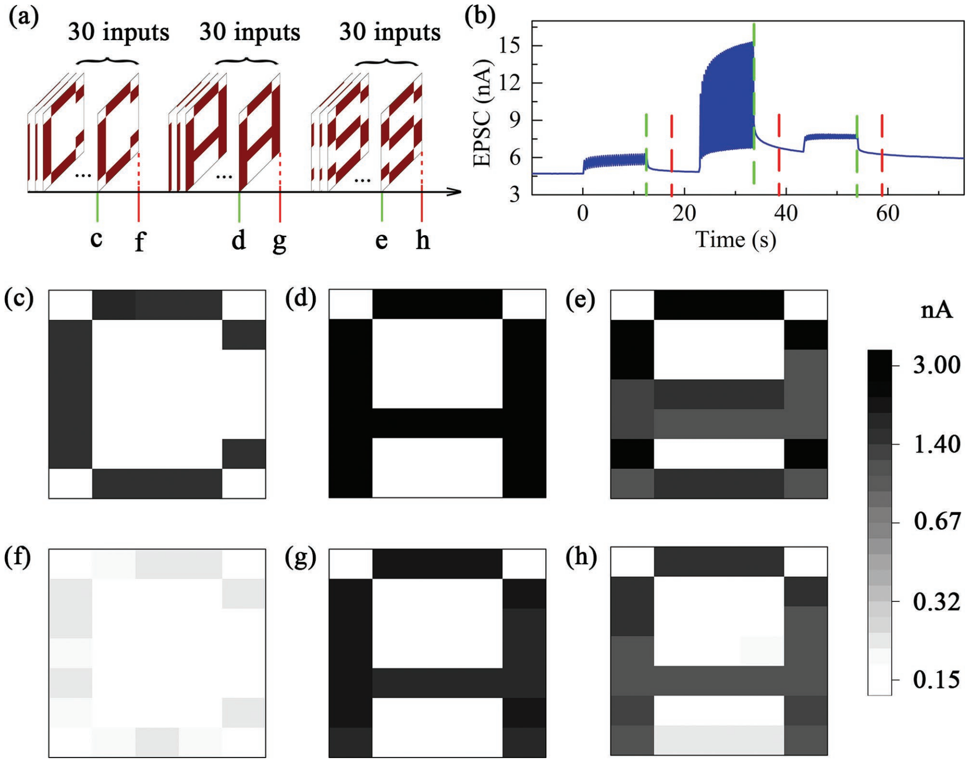

Figure 5. Dynamic process of STM and LTM in a synapse array. a) Images of the letters "C," "A," and "S" were successively inputted into the synapse array each using 30 pulses, with an amplitude of 0.6, 1.8, and 0.6 V (duration time of 210 ms, time interval of 210 ms, and time interval for each stimulus train of 10 s). The positions of the green and red lines represent the moments of the last pulse and 5 s after the last pulse, respectively. b) Typical EPSC curve corresponds to the pixel in the first row and the second column of the synapse array. c–e) Images of "C," "A," and "S" just at the last pulse for inputting letters corresponding to the green line time in (a). f–h) Images of "C," "A," and "S" at the moment correspond to the red line time in (a) which is 5 s after the last pulse. The letters "C" and "S" were memorized in STM mode, and the letter "A" was memorized in LTM mode.

long-term EPSC occurs which can persist for dozens of seconds after the last pulse. In other words, the excitatory current of the letter "A" still occurs after the last pulse of the letter "S" representing a STM process. To demonstrate the memorization and forgetting process in a more intuitive way, Figure 5c–e shows the images for "C," "A," and "S" corresponding to the moments indicated by green lines in Figure 5a, while Figure 5f–h shows the images for the moments indicated by red lines in Figure 5a. The gray level of the images represents the change of EPSCs. The letter "C" temporarily appears (Figure 5c) but quickly becomes almost indistinguishable (Figure 5f), which suggests STM. The letter "A" remains clearly observable, for both the last pulse (Figure 5d) and 5 s after last pulse (Figure 5g). This is due to its LTM property, induced by a high gate bias. Because of LTM of the letter "A," the letter "S" with STM property is unclear (Figure 5e), whereas a clear letter "A" reappears (Figure 5h). Overall, the result from our synaptic transistor correlates well with the short-term and long-term memory in biological synapses.

STDP as a basis for the Hebbian synaptic learning rule has been demonstrated in various neural networks for a wide range of species from insects to humans. Asymmetric STDP appears to be the most dominant form in many systems.[20,44–46] It describes the change of synaptic weight in response to the time difference between the occurring spikes at the pre- and post-neurons ($\Delta t = t_{\mathrm{pre}} - t_{\mathrm{post}}$).[47] If the presynaptic spike precedes the postsynaptic spike within a narrow time window, long-term potentiation is induced. If the order is reversed, long-term depression occurs. Here, we demonstrate that WO_3 synaptic transistor has a STDP function. A multiplexer is usually used to convert the pre- and post-neuron spikes to study STDP, with the output terminals connected to the gate electrode (Figure S15 and Note S2, Supporting Information).[17] The logic of a multiplexer is shown in Table S2 (Supporting Information). A typical asymmetric STDP induced by temporal correlations of pre- and postneuron spikes was obtained (Figure S16, Supporting Information). The magnitude of change in the EPSCs is proportional to the time difference. It can be fitted with an exponential function $\Delta W = A \times e^{(-\Delta t/\tau)} + b$ in each part.[46] The characteristic relaxation times τ are 528.3 and −770.5 ms for potentiation and depression, respectively. The successful demonstration of STDP provides a step forward to realize brain-like processing in WO_3-based synapses.

In summary, we designed an electrolyte-gated synaptic transistor using WO_3 films. Measurements such as electrical transport, XPS, Raman, SIMS, and transmission spectroscopy clarified that both the electrostatic effect induced by EDL and electrochemical effect related with the hydrolysis reaction can modulate the channel conduction. Which effect dominates depends on the gate voltage amplitude. Our results provide clear experimental evidences for STP and LTP behavior in one synaptic transistor using the electrostatic and electrochromic effects, respectively. The feature, that the transition from STM to LTM can be controlled by different gate voltage amplitudes, is useful to simulate the selective activation of neurons in the parietal cortex as a function of attention.[9] In addition, the important synaptic learning rule STDP has been demonstrated in this WO_3 transistor. The proposed synaptic electrolyte-gated transistor may be promising for future synaptic electronics.

Experimental Section

Sample Preparation: Epitaxial WO_3 thin films with a thickness of 30 nm were grown on (001) $LaAlO_3$ substrates (MTI Ltd.) using pulsed laser deposition (PLD) with a 308 nm XeCl excimer laser, an energy density of ≈1 J cm^{-2} and a repletion rate of 2 Hz. The target was prepared with WO_3 powder of 99.99% purity (Sigma-Aldrich) and sintered at 950 °C for 20 h. During the deposition, the temperature was kept at 450 °C with oxygen pressure of 30 Pa.

Device Fabrication: The thin films were patterned into a Hall-bar channel with a coplanar gate structure using standard photolithography and argon-ion etching. The channel size was 500 μm × 50 μm. The 3 nm Cr adhesion layer followed by a 100 nm Au layer were deposited via thermal evaporation as electrodes. An overlayer of a hard-baked photoresist was used as protection layer to prevent electric leakage between gate and source electrode. The device was completed by dropping an ionic liquid DEME-TFSI (Kanto Chemical Co.) on the channel and gate electrode.

Sample Characterization: XRD measurements were performed using a Rigaku SmartLab instrument. A commercial AFM system (Asylum Research MFP3D) was used for the surface morphology measurements. The chemical states of the WO_3 thin films were evaluated using XPS (ThermoScientific EscaLab 250 Xi). The binding energy was referenced against C 1 s at 284.6 eV for all original data. Raman spectroscopy was performed using a Horiba Jobin Yvon LabRAM HR-800 Raman microscopy (λ = 532 nm, power = 1 mW, beam spot = 1 μm) under ambient conditions. The optical transmission spectrum was recorded with a Cary 5000 UV–vis–NIR spectrophotometer. In order to find the relationship between hydrogen concentration and gating voltages, a TOF-SIMS system (ION-TOF Gmbh) was used to identify the depth profiles of protons.

Electrical Measurement: The electrical characteristics of WO_3 devices were measured using a Keithley 4200 semiconductor parameter analyzer with source measurement unit (SMU) in a Lakeshore probe station under ambient conditions. For the transfer curves, the sweeping rate was ≈2 mV s^{-1}. The measurements for temperature-dependent sheet resistance and Hall were done with a Keithley 2182 Nanovoltmeter and a 2400 Sourcemeter in PPMS (Quantum Design Ltd.).

Supporting Information

Supporting Information is available from the Wiley Online Library or from the author.

Acknowledgements

J.-T.Y. and C.G. contributed equally to this work. This work was supported by National Key R&D Program of China (No. 2017YFA0303604), the National Basic Research Program of China (Nos. 2014CB921001 and 2014CB921003), the National Natural Science Foundation of China (Nos. 11674385, 11721404, and 11404380), the Key Research Program of Frontier Sciences CAS (No. QYZDJSSW-SLH020), the Youth Innovation Promotion Association of CAS (No. 2018008), and the Strategic Priority Research Program (B) of the Chinese Academy of Sciences (No. XDB07030200).

Conflict of Interest

The authors declare no conflict of interest.

Keywords

artificial synapse, electrolyte gating, synaptic transistor, tungsten oxide films

Received: March 9, 2018
Revised: June 1, 2018
Published online:

[1] P. Yao, H. Wu, B. Gao, S. B. Eryilmaz, X. Huang, W. Zhang, Q. Zhang, N. Deng, L. Shi, H.-S. P. Wong, H. Qian, *Nat. Commun.* **2017**, *8*, 15199.
[2] M. M. Najafabadi, F. Villanustre, T. M. Khoshgoftaar, N. Seliya, R. Wald, E. Muharemagic, *J. Big Data* **2015**, *2*, 1.
[3] O. Russakovsky, J. Deng, H. Su, J. Krause, S. Satheesh, S. Ma, Z. Huang, A. Karpathy, A. Khosla, M. Bernstein, A. C. Berg, K. F. Li, *Int. J. Comput. Vis.* **2015**, *115*, 211.
[4] S. B. Eryilmaz, D. Kuzum, S. Yu, H.-S. P. Wong, *Tech. Dig. - Int. Electron Devices Meet.*, **2015**, 4.1.1-4.
[5] R. Ananthanarayanan, S. K. Esser, H. D. Simon, D. S. Modha, in *Proc. Conf. High Performance Computing Networking, Storage and Analysis*, IEEE, Portland, Oregon **2009**, pp. 1–12.
[6] Z. Wang, L. Wang, M. Nagai, L. Xie, M. Yi, W. Huang, *Adv. Electron. Mater.* **2017**, *3*, 1600510.
[7] D. Kuzum, S. Yu, H. P. Wong, *Nanotechnology* **2013**, *24*, 382001.
[8] W. Banerjee, Q. Liu, H. B. Lv, S. B. Long, M. Liu, *Nanoscale* **2017**, *9*, 14442.
[9] D. Purves, G. J. Augustine, D. Fitzpatrick, W. C. Hall, A.-S. LaMantia, J. O. McNamara, S. M. Williams, *Neuroscience*, 3rd ed., Sinauer Associates, Sunderland, MA **2004**.
[10] T. Ohno, T. Hasegawa, T. Tsuruoka, K. Terabe, J. K. Gimzewski, M. Aono, *Nat. Mater.* **2011**, *10*, 591.
[11] M. Prezioso, F. Merrikh-Bayat, B. D. Hoskins, G. C. Adam, K. K. Likharev, D. B. Strukov, *Nature* **2015**, *521*, 61.
[12] S. H. Jo, T. Chang, I. Ebong, B. B. Bhadviya, P. Mazumder, W. Lu, *Nano Lett.* **2010**, *10*, 1297.
[13] A. Chanthbouala, V. Garcia, R. O. Cherifi, K. Bouzehouane, S. Fusil, X. Moya, S. Xavier, H. Yamada, C. Deranlot, N. D. Mathur, M. Bibes, A. Barthélémy, J. Grollier, *Nat. Mater.* **2012**, *11*, 860.
[14] T. Tuma, A. Pantazi, M. L. Gallo, A. Sebastian, E. Eleftheriou, *Nat. Nanotechnol.* **2016**, *11*, 693.
[15] M. A. Zidan, J. P. Strachan, W. D. Lu, *Nat. Electron.* **2018**, *1*, 22.
[16] F. Zuo, P. Panda, M. Kotiuga, J. Li, M. Kang, C. Mazzoli, H. Zhou, A. Barbour, S. Wilkins, B. Narayanan, M. Cherukara, Z. Zhang, S. K. R. S. Sankaranarayanan, R. Comin, K. M. Rabe, K. Roy, S. Ramanathan, *Nat. Commun.* **2017**, *8*, 240.
[17] J. Shi, S. D. Ha, Y. Zhou, F. Schoofs, S. Ramanathan, *Nat. Commun.* **2013**, *4*, 2676.
[18] L. Q. Zhu, C. J. Wan, L. Q. Guo, Y. Shi, Q. Wan, *Nat. Commun.* **2014**, *5*, 3158.
[19] C. S. Yang, D. S. Shang, N. Liu, G. Shi, X. Shen, R. C. Yu, Y. Q. Li, Y. Sun, *Adv. Mater.* **2017**, *29*, 1700906.
[20] W. Xu, S.-Y. Min, H. Hwang, T.-W. Lee, *Sci. Adv.* **2016**, *2*, e1501326.
[21] Y. van de Burgt, E. Lubberman, E. J. Fuller, S. T. Keene, G. C. Faria, S. Agarwal, M. J. Marinella, A. A. Talin, A. Salleo, *Nat. Mater.* **2017**, *16*, 414.
[22] Y. H. Liu, L. Q. Zhu, P. Feng, Y. Shi, Q. Wan, *Adv. Mater.* **2015**, *27*, 5599.

[23] S. Z. Bisri, S. Shimizu, M. Nakano, Y. Iwasa, *Adv. Mater.* **2017**, *29*, 1607054.
[24] J. T. Yang, C. Ma, C. Ge, Q. H. Zhang, J. Y. Du, J. K. Li, H. Y. Huang, M. He, C. Wang, S. Meng, L. Gu, H. B. Lu, G. Z. Yang, K. J. Jin, *J. Mater. Chem. C* **2017**, *5*, 11694.
[25] M. Wang, S. Shen, J. Ni, N. Lu, Z. Li, H.-B. Li, S. Yang, T. Chen, J. Guo, Y. Wang, H. Xiang, P. Yu, *Adv. Mater.* **2017**, *29*, 1703628.
[26] X. Leng, J. Pereiro, J. Strle, G. Dubuis, A. T. Bollinger, A. Gozar, J. Wu, N. Litombe, C. Panagopoulos, D. Pavuna, I. Božović, *NPJ Quantum Mater.* **2017**, *2*, 35.
[27] S. G. Altendorf, J. Jeong, D. Passarello, N. B. Aetukuri, M. G. Samant, S. S. P. Parkin, *Adv. Mater.* **2016**, *28*, 5284.
[28] Z. Wang, S. Joshi, S. E. Savel'ev, H. Jiang, R. Midya, P. Lin, M. Hu, N. Ge, J. P. Strachan, Z. Li, Q. Wu, M. Barnell, G.-L. Li, H. L. Xin, R. S. Williams, Q. Xia, J. J. Yang, *Nat. Mater.* **2017**, *16*, 101.
[29] C. Ge, K.-J. Jin, L. Gu, L.-C. Peng, Y.-S. Hu, H.-Z. Guo, H.-F. Shi, J.-K. Li, J.-O. Wang, X.-X. Guo, C. Wang, M. He, H.-B. Lu, G.-Z. Yang, *Adv. Mater. Interfaces* **2015**, *2*, 1500407.
[30] N. Lu, P. Zhang, Q. Zhang, R. Qiao, Q. He, H.-B. Li, Y. Wang, J. Guo, D. Zhang, Z. Duan, Z. Li, M. Wang, S. Yang, M. Yan, E. Arenholz, S. Zhou, W. Yang, L. Gu, C. W. Nan, J. Wu, Y. Tokura, P. Yu, *Nature* **2017**, *546*, 124.
[31] P. Grey, L. Pereira, S. Pereira, P. Barquinha, I. Cunha, R. Martins, E. Fortunato, *Adv. Electron. Mater.* **2016**, *2*, 1500414.
[32] T. H. Fleisch, G. J. Mains, *J. Chem. Phys.* **1982**, *76*, 780.
[33] J. I. Jeong, J. H. Hong, J. H. Moon, J.-S. Kang, Y. Fukuda, *J. Appl. Phys.* **1996**, *79*, 9343.
[34] M. D. Hampton, D. V. Schur, S. Y. Zaginaichenko, V. I. Trefilov, *Hydrogen Materials Science and Chemistry of Metal Hydrides*, NATO Science Series, Vol. *71*, Kluwer Academic, London **2002**, pp. 405–414.
[35] R. F. Garcia-Sanchez, T. Ahmido, D. Casimir, S. Baliga, P. Misra, *J. Phys. Chem. A* **2013**, *117*, 13825.
[36] E. Cazzanelli, C. Vinegoni, G. Mariotto, A. Kuzmin, J. Purans, *Solid State Ionics* **1999**, *123*, 67.
[37] P. Yang, P. Sun, Z. Chai, L. Huang, X. Cai, S. Tan, J. Song, W. Mai, *Angew. Chem., Int. Ed. Engl.* **2014**, *53*, 11935.
[38] S.-H. Lee, H. M. Cheong, J.-G. Zhang, A. Mascarenhas, D. K. Benson, S. K. Deb, *Appl. Phys. Lett.* **1999**, *74*, 242.
[39] L.-A. Kong, J. Sun, C. Qian, Y. Fu, J. Wang, J. Yang, Y. Gao, *Org. Electron.* **2017**, *47*, 126.
[40] G. Indiveri, E. Chicca, R. Douglas, *IEEE Trans. Neural Netw.* **2006**, *17*, 211.
[41] J. J. Yang, D. B. Strukov, D. R. Stewart, *Nat. Nanotechnol.* **2013**, *8*, 13.
[42] D. C. Rubin, A. E. Wenzel, *Psychol. Rev.* **1996**, *103*, 734.
[43] G. Liu, C. Wang, W. Zhang, L. Pan, C. Zhang, X. Yang, F. Fan, Y. Chen, R.-W. Li, *Adv. Electron. Mater.* **2016**, *2*, 1500298.
[44] N. Caporale, Y. Dan, *Annu. Rev. Neurosci.* **2008**, *31*, 25.
[45] G. Q. Bi, M. M. Poo, *J. Neurosci.* **1998**, *18*, 10464.
[46] G. Q. Bi, M. M. Poo, *Annu. Rev. Neurosci.* **2001**, *24*, 139.
[47] W. He, K. Huang, N. Ning, K. Ramanathan, G. Li, Y. Jiang, J. Y. Sze, L. Shi, R. Zhao, J. Pei, *Sci. Rep.* **2014**, *4*, 4755.